RSC Advances

PAPER

View Article Online
View Journal | View Issue

Cite this: *RSC Adv.*, 2024, **14**, 24447

Highly efficient recyclable bismuth nanocatalysts fabricated using a facile one-step aqueous method for faster reduction of azo dye contaminants†

Md. Ataur Rahman,[a] Md. Abdur Rahman,[*a] Md. Ahasanur Rabbi,[b] Masud Rana,[c] Md. Rabiul Karim,[a] M. A. Jalil Miah[a] and Hasan Ahmad[a]

Easily accessible robust synthesis of metallic nanoparticles (NPs) and their colloidal stabilization *via* successive surface functionalization with desired molecules are crucial for catalytic applications. In this research, tannic acid (TA)-functionalized bismuth (Bi)-based novel NPs were prepared *via* a simple *in situ* aqueous reduction of Bi^{3+} ions for the catalytic reduction of azo groups. The synthesis, morphology, and structure of Bi/TANPs were confirmed through spectroscopic, electron microscopic and X-ray diffraction analyses. The Bi/TANPs comprise Bi, carbon, oxygen and sodium as building components and possess a high negative surface charge of −58 mV, colloidal dispersity, thermal stability and crystalline structure. The Bi/TANPs are almost spherical shaped with an average diameter of 33 nm. The surface of the catalyst is mesoporous with a high specific surface area of 267 $m^2\ g^{-1}$. The designed Bi/TANPs exhibit pH-specific affinity for azo dye molecules and reduced azo moieties in the presence of aqueous $NaBH_4$ without requiring any hydrogen gas supply. The catalytic reduction efficiencies of Bi/TANPs against methylene blue and Congo red are almost 100%. These reduction reactions are very fast owing to the presence of TA moieties on the catalyst surface, which facilitate direct electron transfer to azo groups, and follow a pseudo-first-order kinetic model. The catalyst is mechanically recyclable, and shows a minimal loss (<3%) of its initial efficiency until the fifth cycle. This study not only developed an efficient catalyst for the remediation of azo dye-contaminated water, but also offers novel insights into the synergistic effects of TA and glycerin on the reduction mechanism of aqueous Bi^{3+} ions and the concomitant colloidal stabilization of Bi NPs.

Received 25th June 2024
Accepted 15th July 2024

DOI: 10.1039/d4ra04625k

rsc.li/rsc-advances

1. Introduction

Global progress in industrialization has led to critical issues of environmental contamination.[1] Presently, industries are using numerous chemicals to enhance the lifespan, performance, stability, and attractive features of end-products.[1–3] Among other chemicals, synthetic azo dyes are broadly used in many sectors, namely, plastic, cosmetic, textile dyeing, printing, pharmaceutical, rubber, adhesive, paint, paper, board and food processing industries,[1–6] because they possess versatile aqueous solubility, exceptional binding capacity, and attractive colors.[2–4] Industries exploit a large volume of sweet water to attach azo dyes to products to meet the global demands. Because of the process inefficiency of industries, only minute amounts of dyeing agents (5–15%) are being actively attached to desired products,[1,2] while the major part is drained as a large volume of soluble azo dye-contaminated water into local waterbodies and even open environments.[4–6] In recent years, azo dyes have caused serious environmental problems.[7] For instance, azo dyes are considered one of the substantial environment pollutants due to their complex structure and composition, versatile water solubility, high opacity, very slow degradability, high tenacity, and high residual toxicity.[5–7] Water is a fundamental component that not only helps sustain lives on the earth but also plays crucial roles in every single aspect of life. However, contaminated water raises significant health concerns, including short-term illnesses such as dysentery, diarrhea, nausea, anxiety, allergy, vomiting, typhoid, and cytotoxicity and some acute ailments such as asthma and cancers.[1–7]

In addition, undesirable exposure to these harmful azo dyes not only impacts our vital organs such as the kidney, liver, pancreas, and lungs but also poses a serious threat to the safe survival on earth. For example, Congo red (CR) is a benzidine-based azo dye having two azo groups. Benzidine is a known human carcinogen that cannot be metabolized, which is also

[a]*Polymer Colloids and Nanomaterials Research Laboratory, Department of Chemistry, Faculty of Science, University of Rajshahi, Rajshahi 6205, Bangladesh. E-mail: arahman@ru.ac.bd*

[b]*BCSIR Laboratories, Rajshahi, Bangladesh*

[c]*Department of Environment and Energy Engineering, Chonnam National University, Gwangju 61186, South Korea*

† Electronic supplementary information (ESI) available. See DOI: https://doi.org/10.1039/d4ra04625k

poisonous to many other organisms. Due to major health concerns, CR is forbidden in many countries. However, CR is still common in many developing nations as well as third world countries. Another azo dye named methylene blue (MB) is a salt of organic chloride, used in silk, wood, and linen fabric-processing industries.[4,8] Although MB has significant importance in various fabric processing activities, it can be highly toxic to humans, causing fatal diseases such as respiratory failure, severe burns, skin irritation and even cancer.[8,9] Additionally, azo dyes are often resistant to photo-thermal, chemical and biodegradation under aerobic conditions, as they retain their chemical, thermal, and optical stability, and complex aromatic structures.[1,7,8] These color compounds are quite noticeable and unpleasant even at extremely low concentrations in water.[10]

For removing these azo dyes from industrial effluents, various strategies, namely, adsorption, advanced oxidation, anaerobic and aerobic treatments, ultrafiltration, biological and coagulation methods have been used.[5,7] However, these methods are often ineffective, expensive and less feasible for practical applications.[1] On the contrary, catalytic reduction is a newly developed technique, which converts azo dyes into colorless hydrogenated products that are more easily accumulated by environments.[1–3,5] Even some industrially important raw materials are being synthesized by the reduction of azo dyes like CR and methylene blue (MB) for use in agrochemical, medicine, and anticorrosive coating formulation industries.[6,7,11] To synthesize such raw materials, numerous metal catalysts including Pt, Au, Ag, Pd, Ru, Rh, Cu and their various compounds have been employed to accelerate the reduction of azo dyes in the presence of $NaBH_4$.[12–19] However, the precursors of these metal catalysts are not cost-effective, require multistep preparative procedures, use relatively expensive toxic reagents and solvents, and less feasible for real-time recyclable and practical applications.[16] Therefore, it is highly essential to design and develop easily accessible none noble metal-based alternative catalysts that are highly efficient, fast active, recyclable, low cost, and nontoxic to all living species as well as to the environment.[20]

Among others none noble metallic nanoparticles (NPs), Bi NPs are more attractive candidate because they have exceptional thermal conductivity; high magneto-resistance; anisotropic electronic structure; high value of LD_{50}; and minimal residual impacts on mammals, aquatic lives and even microbes.[21,22] In addition, semi-metallic Bi-based products can be transformed into semiconductor-like photocatalysts.[21–24] Hence, Bi-based compounds have recently been used in agriculture, pharmaceuticals, cosmetics, biotechnology and catalysis. Because of minimal toxicity, BiNPs have also been used in versatile theranostics for many lethal diseases such as cancers and life-threatening infections, and as high-contrast imaging agents in X-ray computed tomography.[22–26] Currently, various methods such as photochemical, heat-induced decomposition, chemical reduction, and mechanochemical methods are developed for the preparation of BiNPs.[24–27] For example, Warren *et al.* have synthesized BiNPs *via* photothermal decomposition of organo-Bi precursors.[28] However, this approach needs expensive organo-Bi precursors and very vigorous preparative protocols, which constrained its application potentials in diverse fields, while mechanochemical synthesis involves laser ablation and sonicating exfoliation, generally very hard to afford, and often needs a large quantity of Bi-compounds as precursor materials. In addition, the synthesis procedure consumes high energy and requires specifically designed expensive devices such as high-powered electrothermal equipment. Wiesner *et al.* employed a photochemical reaction for the synthesis of BiNPs. In their preparative protocol, they exposed the precursors to UV light to form NPs *via* a photochemical reaction having an extended reaction duration of 24 h.[27]

Alternatively, the chemical reduction in the solution phase *via* microwave-assisted procedures and solvothermal routes have received more attention in recent years. These methods frequently involve reducing Bi-salts in the presence of small molecules, polymers, and surfactants that act as capping ligands.[29–31] For instance, Wang *et al.* prepared nano-sized Bi particles using poly(vinylpyrrolidone) (PVP) as a dispersing agent and $NaBH_4$ as a strong reducing agent in *N*,*N*-dimethylformamide (DMF).[29] Lei *et al.* synthesized Bi nanospheres by reducing Bi nitrate in an ethylene glycol phase in the presence of PVP.[23] Borovikova *et al.* synthesized colloidal BiNPs using β-cyclodextrin and poly(acrylic acid) as capping ligands in the presence of $NaBH_4$.[31] These synthetic protocols are challenging, often require high temperatures, a large amount of organic solvents such as allylamine, alkane thiol, tetrahydrofuran, DMF, and dimethyl sulfoxide. In addition, Bi particles prepared in organic solvents result in diminished morphological purity that mostly requires multi-step post-purification and surface modification *via* tedious solvent and ligand exchange procedures. The obtained particles exhibit poor morphological responses and are often unsuitable for catalytic applications.[30–32]

Aqueous synthesis of BiNPs is rarely reported because Bi-salts are poorly soluble in water.[22,32] Besides, metallic BiNPs are chemically reactive and highly prone to oxidation by moisture and air oxygen.[22,32,33] Therefore, we hypothesize that for the practical application perspective, it is important to develop suitable reduction conditions and concomitant protection strategies that will ensure the facile production of functionalized colloidal BiNPs for faster catalytic reactions. The use of naturally abundant antioxidants, namely, polyphenols in reducing metal ions and stabilizing metal NPs is an interesting research area. Polyphenols have multiple active functionalities that are highly biocompatible and biodegradable and can easily encapsulate metal NPs to prevent their oxidation and aggregation *via* ligation. Among others polyphenolic compounds, tannic acid (TA) is a water-soluble naturally occurring abundant versatile organic compound having 25-phenolic-OH moieties, 10-gallic acid residues and one hydrophobic-core-glucose unit.[34–36] Various food stuffs such as pomegranates, persimmon, nutgalls, red wine, grapes, wattle barks, and tea extracts contain considerable amounts of TA. TA has been used to synthesize various metallic particles.[36] In addition, TA-functionalized metallic NPs showed enhanced colloidal stability and improved catalytic efficiency.[37–39] Dutta *et al.* reported one-step synthesis for the stable colloidal dispersion of

nanostructured nickel (Ni) using TA in ethylene glycol.[40] In another work, Hojat *et al.* prepared TA-modified Fe_3O_4@TA/Ag for reducing azo dyes.[37] Water has an exceptional dielectric constant, high specific heat capacity, high accessibility, affordability and eco-friendly nature.[39–42] Water-based synthetic procedures ensure inherent exceptionalities, namely, improved colloidal stability due to high polarity and enhanced affinity towards adsorbate molecules. In addition, the use of water allows faster product separation and easier catalyst recycling during real-time practical applications. Besides, water may have an impact on the catalytic capabilities, such as by accelerating the kinetics of reaction with increasing specificity.[39,41,42] To the best of our knowledge, there is no report on TA-assisted *in situ* aqueous reduction of Bi^{3+} ions, and formation and stabilization of BiNPs in the literature.

This research guarantees a simple, cost-effective, *in situ* one-step aqueous method for fabricating colloidal, recyclable, user-friendly, nontoxic, and metallic BiNPs using Bi-nitrate, TA and glycerin for faster catalytic applications. Here, both TA and glycerin are water-soluble compounds that enable solubilizing Bi-nitrate in an aqueous medium and act as reducing agents for Bi^{3+} ions and as functionalizing agents for bare BiNPs. TA functionalization to the bare surface of metallic BiNPs enhances colloidal stability, protects from unwanted air oxidation, and reduces undesirable aggregation. TA coating also prevents leaching out of Bi ions *via* forming highly stable chelate complexes during catalytic application under acidic conditions. The reaction parameters were first optimized to establish a direct robust aqueous-phase one-pot procedure to reduce Bi^{3+} ions to form BiNPs in the presence of TA and glycerin. The synthesized Bi/TANPs were characterized using various techniques and examined for the catalytic reduction of aqueous azo dyes in the presence of $NaBH_4$. To optimize the parameters for the catalytic reduction reaction, the effects of the initial concentration of dyes, catalyst contact time, and dispersion pH on the catalytic efficiency were studied. The catalytic activities of Bi/TANPs against the reduction of two model azo dyes, namely, MB and CR were determined in the presence of $NaBH_4$ under optimized conditions. Mechanically recovery and reusability performances of Bi/TANPs were investigated up to the eighth reduction cycle of azo dyes. In addition, the reduction mechanism, reduction kinetics, and reduction efficiency of the newly designed Bi/TANPs have also been compared with other metallic catalysts.

2. Experimental

2.1 Materials

Tannic acid was purchased from Merck KG_aA 64271, Darmstadt, Germany. Bi(III) nitrate pentahydrate ($Bi(NO_3)_3 \cdot 5H_2O$) was purchased from Merck Limited, Worli, Mumbai-400018, India. Congo red, $C_{32}H_{22}N_6Na_2O_6S_2$, (CR) and methylene blue (MB) were purchased from Matheson Coleman and Bell, USA. Glycerin was purchased from LOBA Chem., India. Reagent-grade sodium hydroxide (NaOH), hydrochloric acid (37%), and other chemicals were used as received. Deionized distilled water (DDW) was prepared using a Milli-Q water purification system.

2.2 Aqueous one-step preparation of nanocatalysts

The whole synthetic procedure of Bi/TANPs is shown in Scheme 1. A typical synthetic process is briefly described below: a three-necked round-bottom (RB) flask equipped with a reflux condenser was placed on a thermostat magnetic stirrer. First, 0.1 g of glycerin was taken in a closed beaker. Then, 18.7 g of water was added to the beaker and the solution was swirled well. After that, 0.8 g of TA was added to the solution and solubilized well. Finally, an appropriate amount of $Bi(NO_3) \cdot 5H_2O$ salt was added to the solution and the salt was dissolved by sonication for 1 min under bubbling nitrogen gas. The pH of the solution was adjusted to 11 with dilute aqueous NaOH. The light gray-colored solution was transferred into a three-necked RB flask and it was placed on a thermostat hotplate magnetic stirrer. The temperature was adjusted to 80 °C and the dispersion was stirred at a speed of 350 rpm for 5 h. The initial gray color dispersion turned black and the product was obtained by centrifugation at 4500 rpm. The obtained products were centrifugally washed several times with DDW. Then, the products were dried at 70 °C and stored in a refrigerator for further use. This protocol was repeated several times using different amounts of ingredients to optimize the particle size and the conditions for the reduction reaction of Bi^{3+} ions and

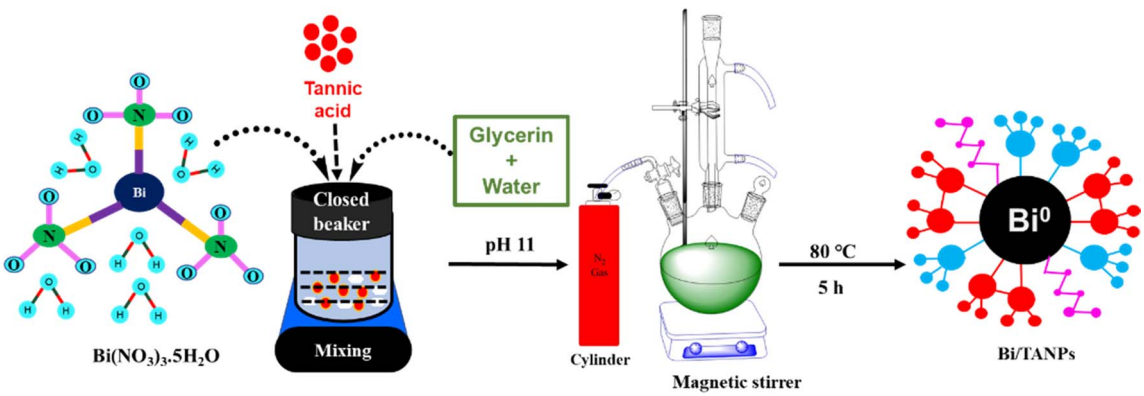

Scheme 1 Schematic of the facile one-pot aqueous synthesis of Bi/TANPs under alkaline conditions at 80 °C.

stabilization. The detailed procedures of these trials are given in Table S1.†

2.3 Instruments

The functionality of Bi/TANPs was determined using a Fourier transform infrared spectrophotometer (PerkinElmer, FTIR-100, USA) in the range of wavenumber from 4000 to 400 cm^{-1}. The elemental surface composition and actual oxidation states of the constituent elements in Bi/TANPs were identified using an X-ray photoelectron emission spectrometer (XPS), ESCALAB250, Thermo Fisher Scientific, USA. The optical behavior of Bi/TANPs was evaluated in the wavelength range of 200–800 nm using a UV-vis spectrophotometer (Lambda 25, PerkinElmer, USA). The thermal characteristics of Bi/TANPs were assessed using a thermogravimetric analyzer (TGA; STA 8000; PerkinElmer, Netherlands). A NICOMP 380 particle sizer (Santa Barbara, California, USA) was used to measure the hydrodynamic average diameter of Bi/TANPs. The crystallinity of Bi/TANPs was detected using an X-ray diffractometer of Rigaku Ultima IV, RINT D/max-kA, Japan. Bi/TANPs were washed and recovered from the dispersion medium using a high-speed centrifuge (TG16-WS, China), while the pH value was adjusted and monitored using a pH meter manufactured by Mettler Toledo Company, MP 220, Switzerland. The specific surface area, pore diameter, and pore volume of Bi/TANPs were measured using a NOVA 3000e instrument, South Korea. The surface morphology, size distribution and elemental composition of the synthesized Bi/TANPs were analyzed using a high-resolution transmission electron microscope (HRTEM) from JEOL, JEM 2100F, Japan and a scanning electron microscope (SEM) combined with an energy-dispersive X-ray (EDX) analyzer from JEOL, Japan. Using the same TEM instrument, SAED and HRTEM data were acquired.

2.4 Catalytic reduction of model azo dyes

The catalytic activities of the Bi/TANP catalyst against the reduction of MB and CR were assessed under different conditions. These reduction reactions were carried out in the presence of a reducing agent, $NaBH_4$ in a 50 mL conical flask. For the catalytic reduction of each MB and CR, 250 mL aqueous dye solution of different concentrations of 40, 60, 80, 100, and 120 mg L^{-1} was prepared. At room temperature, $NaBH_4$ (1.0 mg) was mixed with an aqueous dye solution followed by the addition of Bi/TANPs (0.2 mg) under moderate stirring. The color of the reaction mixture disappeared immediately. About 5 mL of sample solution was taken out at regular intervals. By recording the UV-vis absorption spectra, the progress and kinetics of the catalytic reduction were determined in the wavelength range of 200–800 nm. For calculating the concentrations of MB and CR in the residual mixture, respective absorbances were measured or a calibration standard method was used. A blank experiment without any nanocatalyst was also performed. The reduction percentage ($D\%$), with respect to time was determined using eqn (1):

$$D\% = [(C_0 - C_t)/C_0] \times 100 = [(A_0 - A_t)/A_0] \times 100 \quad (1)$$

where C_0 and A_0 are the initial concentration and absorbance of azo dyes; C_t and A_t are the concentration and absorbance at a specific time interval (t) in seconds, respectively. The kinetic data for this catalytic reduction were fitted with a pseudo-first-order kinetic model given in eqn (2):

$$\ln(C_t/C_0) = \ln(A_t/A_0) = -k_1 t \quad (2)$$

Furthermore, the catalytic performances of Bi/TANPs were determined at different concentrations of MB (40, 60, 80, 100, and 120 mg L^{-1}) and CR (30, 50, 70, and 90 mg L^{-1}) azo dyes in triplicate. The reduction percentages of azo dyes for every single measurement at different concentrations were averaged and shown with the calculated standard error bars. The effect of dispersion pH on the reduction of azo dyes was determined. The reduction time was also assessed at different pH values, namely, 2, 4, 6, 8, 10, and 12 for MB and pH 6, 7, 10, and 12 for the CR solution.

2.5 Recovering catalysts from the reaction medium

Recycling experiments were conducted using suitable amounts of Bi/TANPs and $NaBH_4$ in an aqueous azo dye solution. After the first reduction cycle, the catalyst was collected from the reaction mixture by centrifugation at 5000 rpm and washed with water and an ethanol–water–HCl mixture. The separated catalyst was then dried at 60 °C in an electric oven and reused for next cycles. The experiments were repeatedly continued up to the 8th cycle for both MB and CR. Finally, the catalyst was obtained by centrifugal washing and dried and then the changes that occurred in its structure were observed for recycling use *via* FTIR and XRD measurements.

3. Results and discussion

A facile one-pot aqueous synthesis of Bi/TANPs was performed using bismuth nitrate in an aqueous solution of TA and glycerin under alkaline conditions. The mechanisms for the reductive transformation of Bi^{3+} ions into metallic Bi^0 and the stabilization of BiNPs are schematically shown in Scheme 2. Under basic conditions, TA is partially hydrolyzed to form gallic acid and glucose.[34,36,43,44] These gallic acid moieties lose protons to form phenoxide ions that supply electrons more easily than their non-ionic counterparts and transform into quinone-type structures. The transformations of phenolates into quinones and glucose into gluconic acid allow the aqueous reduction of Bi^{3+} ions into metallic Bi^0. Therefore, TA is believed to work as a mild reducing agent for Bi^{3+} ions. Since TA is a weak reducing agent, glycerin was used as a co-reducing agent. After the nucleation of Bi^0 metal particles, the particle growth process continued until the optimum concentration of reducing agents as well as Bi^{3+} ions was available in the reaction mixture. The formed metallic particles were then stabilized through ligation of multiple chelate-forming moieties present in the structure of TA, gluconic acid, and gallic acid, which can be explained by the hard–soft acid–base theory.[32] For example, the phenolic OH groups present in TA and gallic acid possess enough potentials to bind the metal surface *via* coordination due to the presence

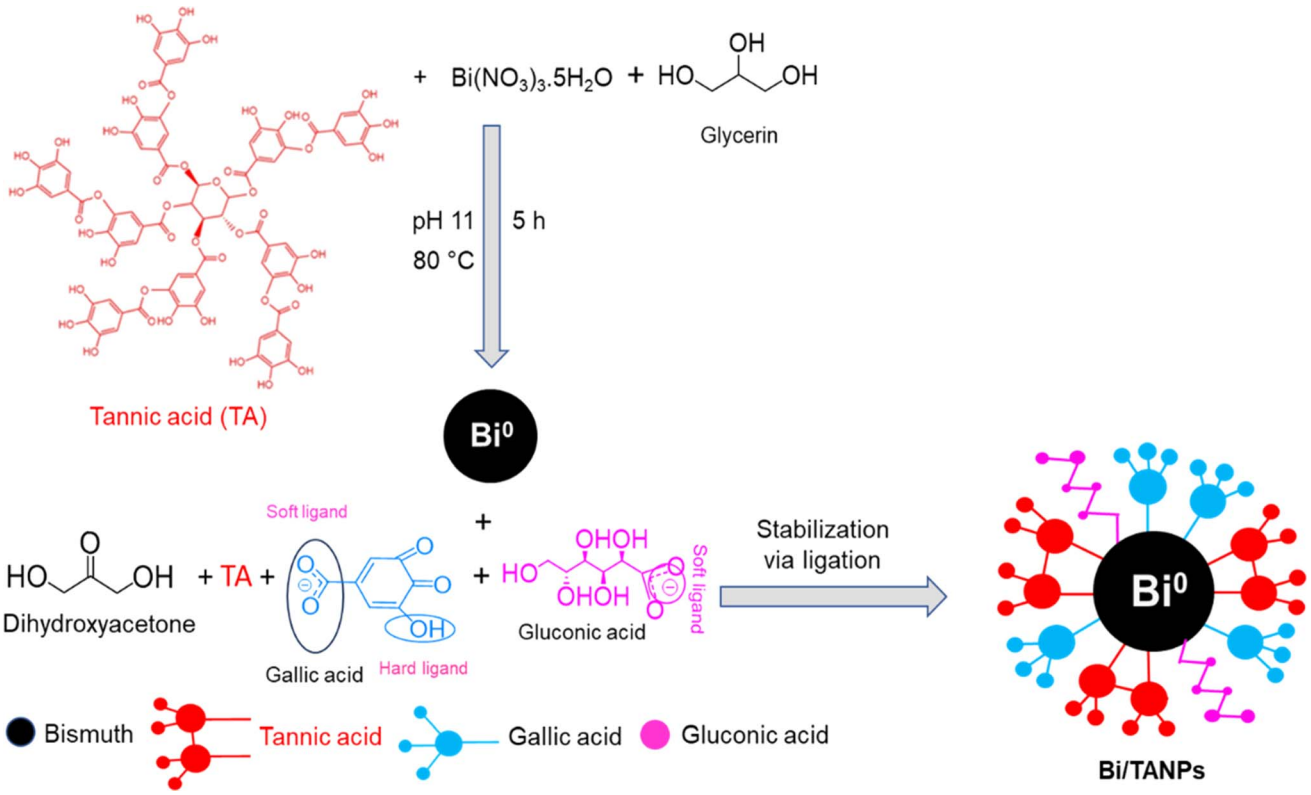

Scheme 2 The possible mechanism for aqueous synergistic one-pot reductive transformation of Bi^{3+} ions into metallic BiNPs and their concomitant colloidal stabilization with TA, its hydrolyzed fragments and glycerin *via* ligation.

of many vacant outer-shell orbitals of metal atoms. Therefore, the bare surface of each BiNP is stabilized *via* the ligation of phenolic OH and COO^- groups of the TA, gluconic acid, and gallic acid moieties.[45] A stable and strong ligation was observed at 80 °C *via* interactions of active functional groups in TA and gallic acid that produced a chemically cross-linked organic network structure with a highly porous Bi/TANP surface.

3.1 Size-shape and surface morphology

The hydrodynamic average diameter and size distribution of Bi/TANPs in the colloidal state were assessed by a dynamic laser scattering method. The hydrodynamic average diameter of Bi/TANPs was 209 nm and the coefficient of variations was 0.320. The hydrodynamic average diameter of the Bi/TANPs is quite high due to the presence of hydrophilic TA molecules and the coexistence of hydration layer on the surface of particles.[21] The particle size, shape, and morphology of the synthesized Bi/TANPs were further analyzed in the dried state using SEM and TEM. As evident from the different resolution of SEM images (Fig. 1a and b), Bi/TANPs exhibited both spherical and irregular shaped and had slight tendency to aggregation due to the post-processing of specimen from their dispersed state to the solid state *via* vacuum drying under reduced pressure. The average particle size was found to be 33 nm. Using the ImageJ program, a histogram plot was generated, which is shown in the inset in Fig. 1a clearly indicating relatively narrow size distribution. The TEM images shown in Fig. 1c and d at different 20 and 10 nm resolutions also revealed a smooth surface with quite spherical shaped Bi/TANPs. The average diameter of Bi/TANPs is about 20 nm. The particle size observed from TEM image analysis is smaller than that measured from the SEM image. The bombardment of samples with high-energy electron beams during TEM observation might have decomposed the TA layer and plausibly formed the agglomerated clusters of Bi/TANPs. In addition, lighter elements such as C, O, and H present in the TA layer cannot scatter the high-energy electron beams and thus mostly passed through these elemental layers and the coating of TA could be transparent.[45–48]

3.2 Crystal structure and surface charge

Powder X-ray diffraction (XRD) profile was used to determine the crystal structure and phase purity of Bi/TANPs at room temperature in the diffraction angle of 2θ values from 10° to 60°. Fig. 2c depicts the XRD pattern of Bi/TANPs. This XRD profile shows some characteristic reflections centered at 27, 33, 34, 44, 50.0 and 56° that are assignable to the lattice planes of (012), (200), (104), (015), (120) and (024) for the rhombohedral structure of Bi unit cells, respectively.[21] All these signal positions for Bi/TANPs are in good agreement with those reported in the literature (JCPDS file number no. 05-0519).[49] The highest intense signal at 27° is in agreement with the (012) family plane, which is a clear indication of the presence of metallic Bi. No bismuth oxide phase is observed on the surface of Bi/TANPs.[21] In addition, the XRD profile also showed two other

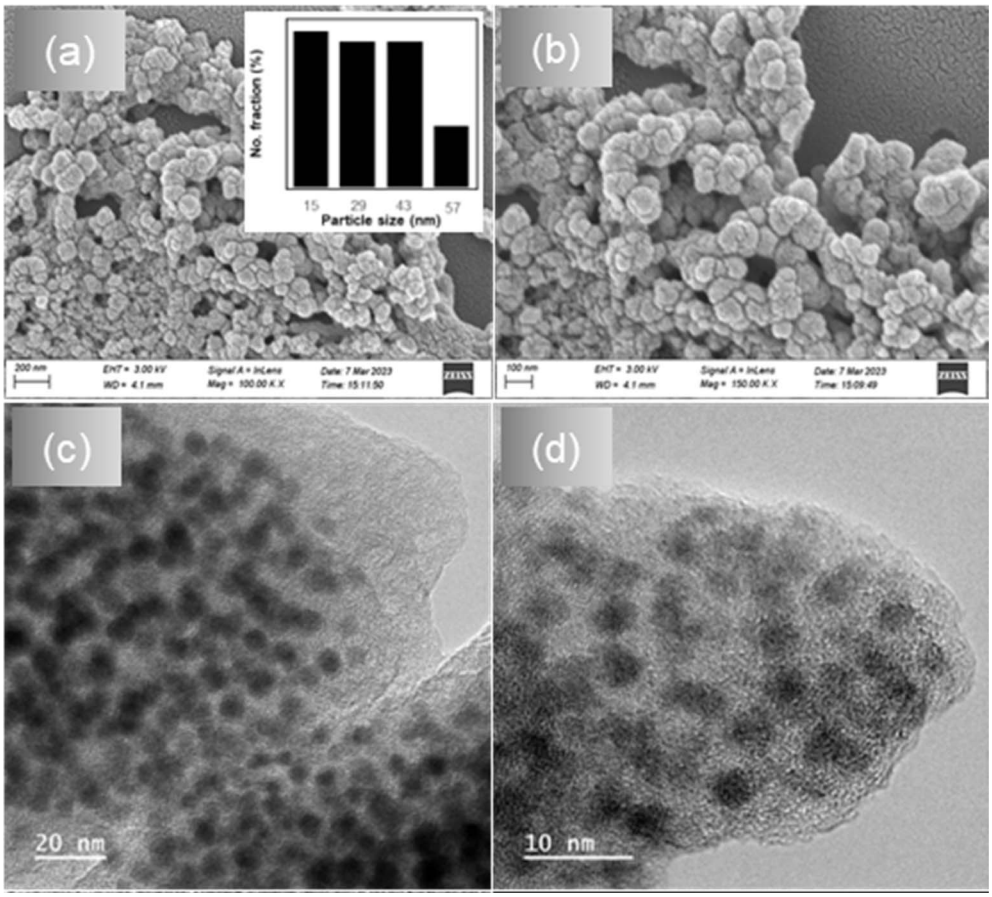

Fig. 1 SEM images: (a) 200 nm and (b) 100 nm. TEM images: (c) 20 nm and (d) 10 nm of Bi/TANPs.

characteristic signals at 33 and 37° corresponding to the (104) and (200) planes respectively for metallic Bi (JCPDS file number no. 65-2366).[21] In Fig. 2a, the high-resolution transmission electron microscopic (HRTEM) image indicates the crystalline structure of Bi/TANPs as well as the lattice fringes with a measured interplanar *d*-spacing of 0.33 nm, which agreed well with the (012) plane of the rhombohedral unit cell of Bi.[21,49] The selected area diffraction (SAED) pattern of Bi/TANPs is shown in Fig. 2b. Three diffused Debye–Scherrer rings were observable, which are characteristic of polycrystalline structure and assignable to the corresponding Braves lattice of (024), (102), and (012) planes.

The zeta potential is one of the most important techniques for assessing the long-term colloidal stability of NPs in dispersion media. The degree of electrostatic attraction as well as repulsion between two distinct charged layers on the surface of particles in a liquid medium was assessed by zeta potential measurement. The particles with a potential greater than +30 mV and less than −30 mV are regarded as stable for the colloidal dispersion irrespective of steric stabilization.[32] Fig. 2d exhibits the zeta potential profile of Bi/TANPs. The zeta potential diagram revealed that the surface of Bi/TANPs is negatively charged and the numerical value of surface potential is −58.6 mV, which clearly demonstrates high colloidal stability of the nanocatalyst.

3.3 Formation and functionality of Bi/TANPs

FTIR spectral analyses were performed to ensure the preparation of the Bi/TANPs. Fig. 3 shows the FTIR spectra of TA, Bi/TANPs and bare-Bi particles. In the FTIR spectrum of TA, a broad band appeared in the region of 3600–3000 cm^{-1} assigned to the characteristic O–H stretching vibrations of polyphenolic-TA and surface-adsorbed water molecules.[34] The absorption band at 1714 cm^{-1} is assigned to the C=O stretching of esteric groups in TA.[34,36] Another band also appeared at 1205 cm^{-1} which is assigned to the phenolic C–O stretching vibrations, and the three sharp peaks at 1540, 1480 and 1330 cm^{-1} are attributed to the C=C stretching vibrations of the aromatic rings.[32] The FTIR spectrum of Bi/TANPs showed a strong and broad absorption band at 3342 cm^{-1} assigned to the O–H groups of physically absorbed water and polyphenolic O–H of TA. The sharp peak at 1688 cm^{-1} is attributed to the bending vibrations of O–H and C–H present in TA. Generally, Bi-oxides provide different stretching and deformation variations in the region of 400–600 cm^{-1}. Herein, a sharp peak appearing at 559 cm^{-1} which is assigned to the Bi–O vibration is due to the ligation of $-CO_2^-$ and Ph–O^- groups of TA towards Bi atoms on the surface of metallic Bi NPs.[50,51] In the FTIR spectrum of Bi/TANPs, the exhibited bands are shifted towards higher frequencies from that of TA.[34] For example, the shiftings

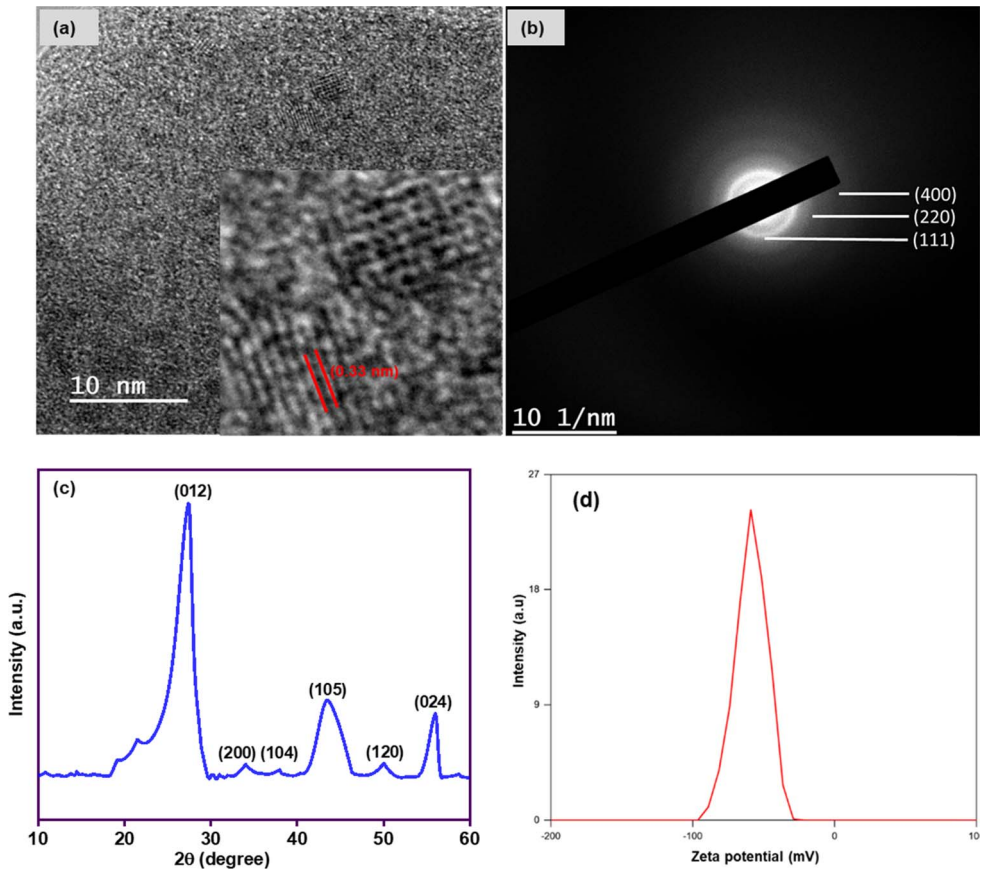

Fig. 2 (a) HRTEM image and (b) SAED pattern of Bi/TANPs. (c) Powder X-ray diffraction pattern of Bi/TANPs measured under ambient conditions. (d) Zeta potential of Bi/TANPs measured in deionized distilled water at 25 °C. Solid content of the dispersion used for zeta potential measurement was 0.02 mg mL^{-1}.

were from 3275 to 3342 cm^{-1} for O–H stretching vibrations, and 1205 to 1268 cm^{-1} for C–O phenolic group stretching vibrations. The C═O stretching is shifted from 1714 cm^{-1} towards the lower wavenumber of 1688 cm^{-1}. The changes in peak positions are suggesting the possible interactions of carboxylate and phenoxide groups of TA and gallic acid towards the surface of metallic-Bi *via* formation of highly stable chelate-complexes.[38] The interaction between the functional moieties and the metal surface was also confirmed by the UV-vis spectra analyses of TA and Bi/TANPs.

3.4 Elemental mappings and surface compositions

Energy-dispersive X-ray spectrum showed that Bi/TANPs are composed of Bi, C, and O as elements, which is shown in Fig. S1a.† To investigate the elemental distributions on the surface of the synthesized Bi/TANPs, combined and individual EDX elemental mapping analyses were performed. The distributions of individual elements, namely, Bi, C, and O present on the surface of Bi/TANPs are clearly depicted in Fig. S1c–e,† respectively. The surface chemical composition was further assessed by using a wide-scan XPS survey spectrum, which is shown in Fig. 4a. The XPS survey spectrum of Bi/TANPs revealed some peaks appearing at 23.7, 26, 164.3 and 158.98 eV, which are assigned to the binding energies of Bi, and the binding energies at 291.71 eV and 538.4 eV are assigned to the C and O atoms, which are the building elements of the Bi/TANPs. The actual oxidation states of the individual elements were determined using the deconvoluted narrow-scan XPS spectrum of the respective elements in Bi/TANPs. The deconvolution of the survey spectrum of C 1s depicted in Fig. 4b exposed three sharp peaks. The predominant peak at 284.5 eV is attributed to the sp^2 hybridized carbon atom of TA. Meanwhile, the supplementary pair of peaks are appearing at higher binding energies of 285 and 288.2 eV, which are assignable to the C–O and O–C═O bonds, respectively.[52] The C 1s peaks correspond to adventitious carbon (AdC) are present on all surfaces with air exposure containing CO_2.[53] As shown in Fig. 4c, the O 1s peaks can be deconvoluted into three peaks at 532.7, 530.9, and 529.7 eV that are assigned to the O–H, O–C and O–Bi bonds, respectively.[21] The Bi 4f region has revealed a well-separated spin orbit interaction splitting (Fig. 4d). The doublet asymmetric sharp peaks at 164.3 and 158.98 eV are assigned to Bi $4f_{5/2}$ and Bi $4f_{7/2}$ of metallic Bi^0.[52] The sharp peaks appearing at 466 and 444 eV are in agreement with the characteristics of Bi^0 $4d_{3/2}$ and Bi^0 $4d_{5/2}$, which are shown in Fig. 4e for metallic Bi^0.[21,53] The signal appearing at 28.8 eV indicates Bi^{3+} $5d_{3/2}$ close to Bi oxide, as

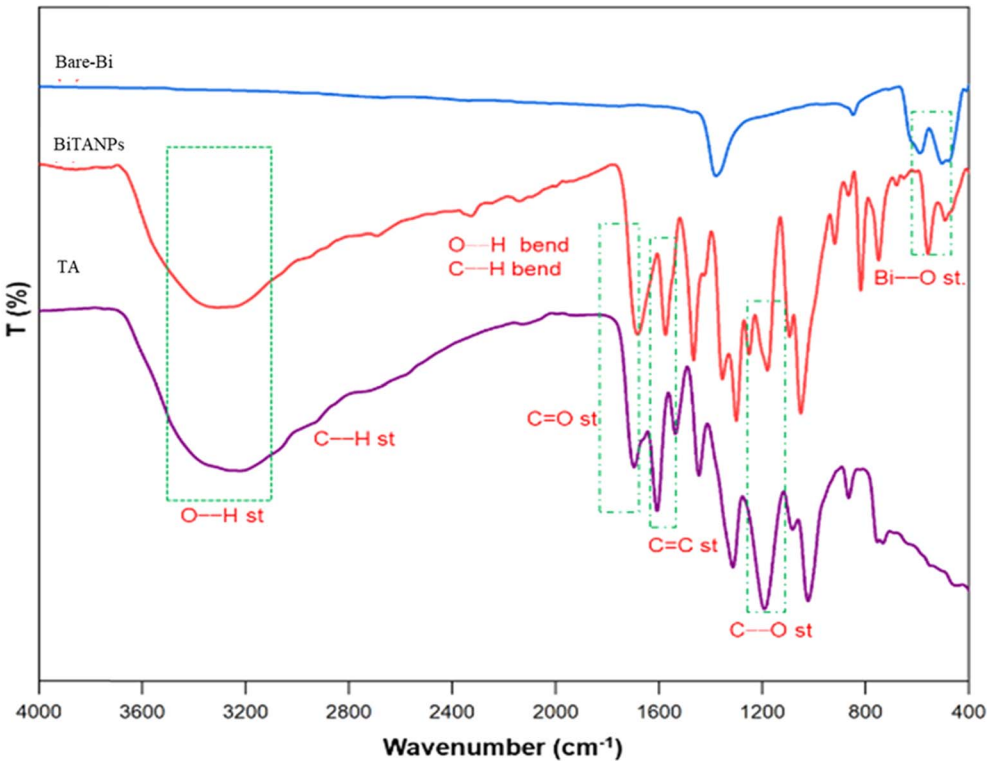

Fig. 3 ATR-FTIR spectra of bare-BiNPs, Bi/TANPs, and TA measured under ambient conditions.

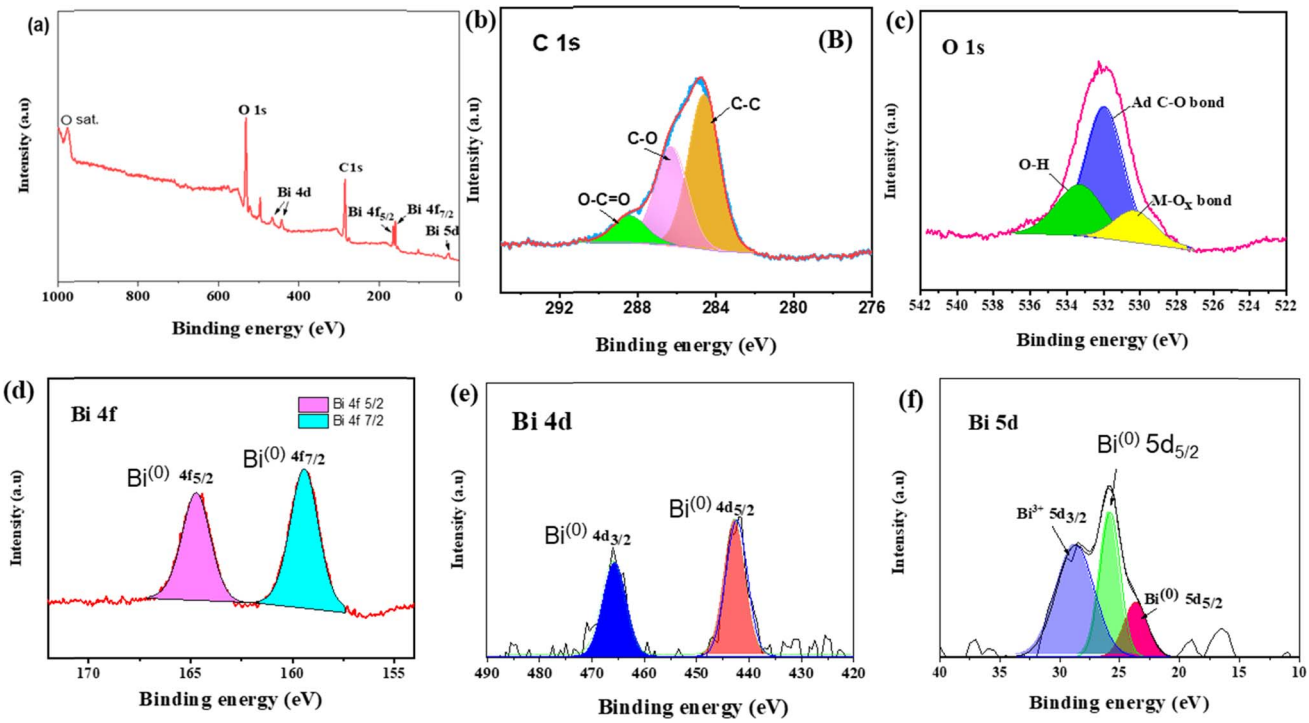

Fig. 4 XPS (a) wide scan survey spectrum of Bi/TANPs and (b–f) core-level narrow-scan spectra of (b) C 1s; (c) O 1s and (d) Bi 4f, (e) Bi 4d and (f) Bi 5d in Bi/TANPs.

shown in Fig. 4f, which revealed the presence of oxide species on the surface of Bi/TANPs due to the successful ligation of phenoxide and carboxylate moieties.[52]

3.5 Optical, thermal properties and surface porosity

Fig. 5a shows the UV-vis spectra of TA and Bi/TANPs. The TA absorption spectrum in the aqueous solution showed two peaks

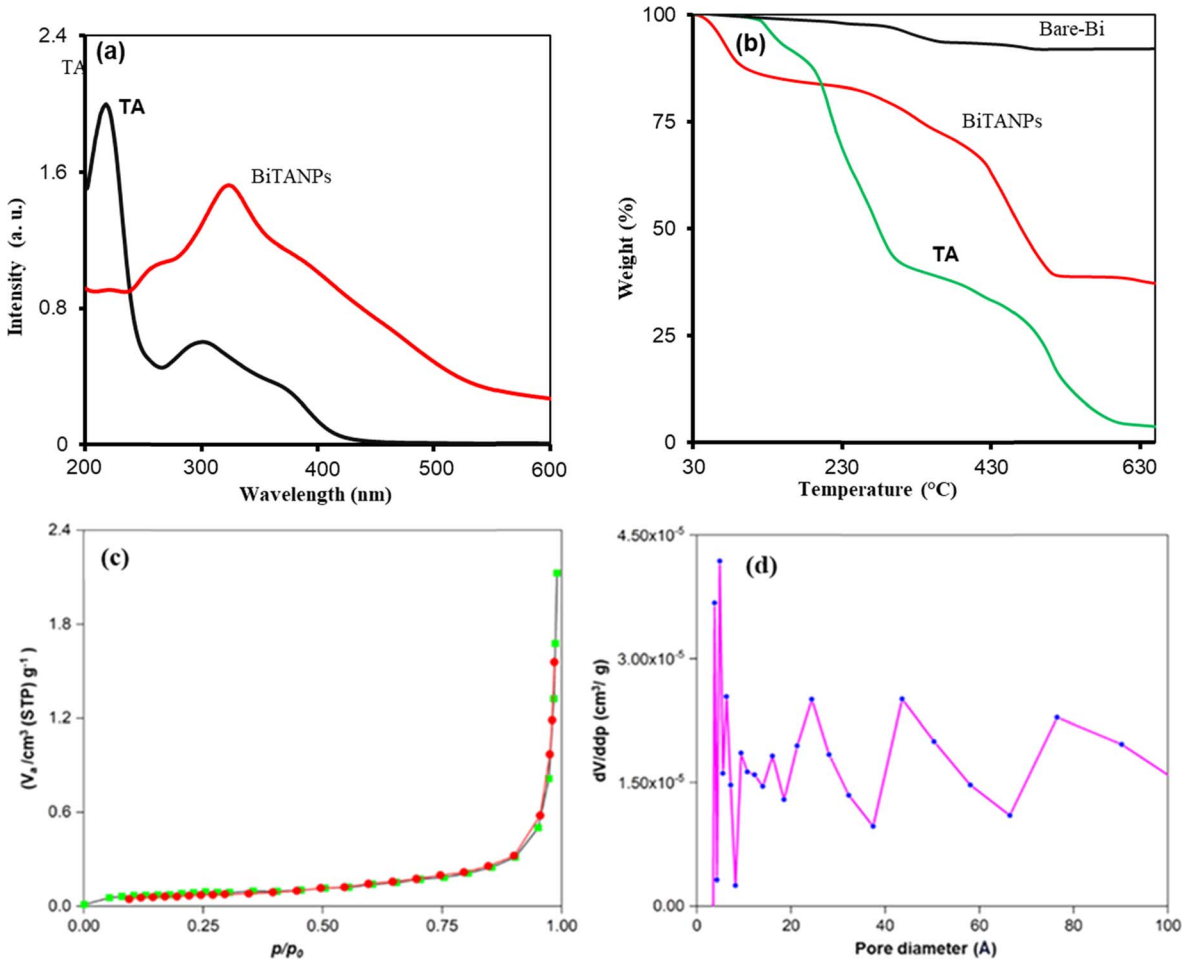

Fig. 5 (a) UV-vis spectra of TA and Bi/TANPs; (b) thermograms of bare-BiNPs, Bi/TANPs and TA; (c) BET-N_2 gas adsorption–desorption isotherm; and (d) BJH pore-size distribution of Bi/TANPs.

at 214 and 276 nm. These are attributed to the $\pi \rightarrow \pi^*$ transition of the aromatic rings and the $n \rightarrow \pi^*$ transition of the carbonyl groups at its neutral state, which are consistent with the spectra of TA given in the literature.[34] When TA is combined with metallic Bi^0 to form Bi/TANPs, the two adsorption peaks are shifted towards 250 and 297 nm. The red-shift of these peaks is due to the plausible change in the electronic environments and structure of chromophores in TA *via* strong interactions between Bi^0 and polyphenolic OH and $-CO_2^-$ groups.[34,36] The conversion of anionic phenolic group into quinone form allowed easier electronic transitions at a relatively low energy, and thus, resulted in red-shifts and the reductive transformation of Bi^{3+} ions into metallic Bi^0.

Fig. 5b shows the thermogravimetric analysis data of bare-Bi, Bi/TANPs, and reference-TA. TGA was performed to evaluate the thermal resilience of the synthesized particles and to determine the proportions of inorganic and organic components integrated within Bi/TANPs. The thermogram of bare-Bi reveals a consistently linear graph, which indicates the outstanding thermal stability of bare Bi (Fig. 5b). The TGA thermograms of Bi/TANPs show a four-stage thermal decomposition zone, where the first zone up to 100 °C represented 2.37% weight loss due to the removal of physiochemically adsorbed water.[47,48] In the second-stage decomposition zone, a comparatively large weight loss of approximately 45% in the 290–580 °C region is due to the decomposition of the respective organic contents. The final decomposition stage between 590 and 700 °C produced a residual weight of 35% for inorganic contents in the Bi/TANPs. While the TGA profile of TA showed five thermal zones, the first is observed between 25 and 126.0 °C, with 2.34% mass loss due to the removal of water and small volatile organic components. At 259 and 304 °C, two major weight loss contributions were observed, which were associated with the degradation of the outer layer of gallic acid units, which accounted for about 50% of the total TA weight. Above 400 °C, the gallic acid units in the inner layer began to break down as well. Its residual mass has been linked to the formation of biochar during the thermal decomposition of TA under nitrogen, and it corresponds to the values reported in the literature.[34] Since the inner aromatic rings are condensed and cross-linked through intramolecular and intermolecular reactions, the majority of the carbon–oxygen-containing functional groups in the glucose central ring and the gallic acid units are reported to be still intact at 700 °C. The nitrogen

adsorption–desorption isotherms were utilized to determine the BET-specific surface area of Bi/TANPs.

Fig. 5c depicts the nitrogen adsorption–desorption isotherm of Bi/TANPs with a hysteresis loop at a relative pressure (P/P_0) near unity. BET analysis revealed that the specific surface area of Bi/TANPs is 267 $m^2\ g^{-1}$. In Fig. 5d, by the BJH method, the average pore diameter of Bi/TANPs was determined to be 4.78 nm. The range of pore diameter is between 2 and 50 Å, which indicates that the synthesized particles are mesoporous in nature.[52–55] The BJH pore distribution method suggests that the pore size distribution of Bi/TANPs is quite well defined.

3.6 Optimization of conditions for catalytic reduction

Reduction reaction parameter optimization study revealed that the catalyst showed pH-specific variable efficiency with changing reaction parameters such as time, concentration, and pH under room temperature, which are clearly depicted in Fig. S2 and S3.† The optimized conditions are used for the catalytic reduction of MB and CR in the presence of catalysts and reducing agents that are briefly delineated below.

3.6.1 Catalytic reduction of model azo dye, MB. The catalytic reduction of MB was assessed in the presence of Bi/TANPs using a reducing agent ($NaBH_4$). Fig. 6a–d show the optical images of the time-dependent change in MB color. The structure of MB gradually changed into Leuco-MB (LMB, colorless). The reductive degradation of MB (Fig. 6a) using only $NaBH_4$ took 120 min to be completed and the color was unchanged just after the addition of reagent.[56] When the Bi/TANP catalyst was used in the reaction mixture, the degradation speed dramatically increased. The intense blue color of MB started to diminish with increasing time and the discoloration was completed within 40 s, as depicted in Fig. 6b–d. The reduction kinetics of MB was also monitored using a UV-vis spectrophotometer. MB showed two absorption peaks at 664 and 614 nm in the aqueous medium.[57] It is observed that the presence of Bi/TANPs produced a quick drop in the absorption intensity of MB solution with increasing time. The Bi/TANP catalyst helped to transfer the electrons from the donor, BH_4^- to the acceptor, MB. With regard to Bi/TANPs, BH_4^- ions are nucleophilic, while MB is an electrophilic compound because the latter receives

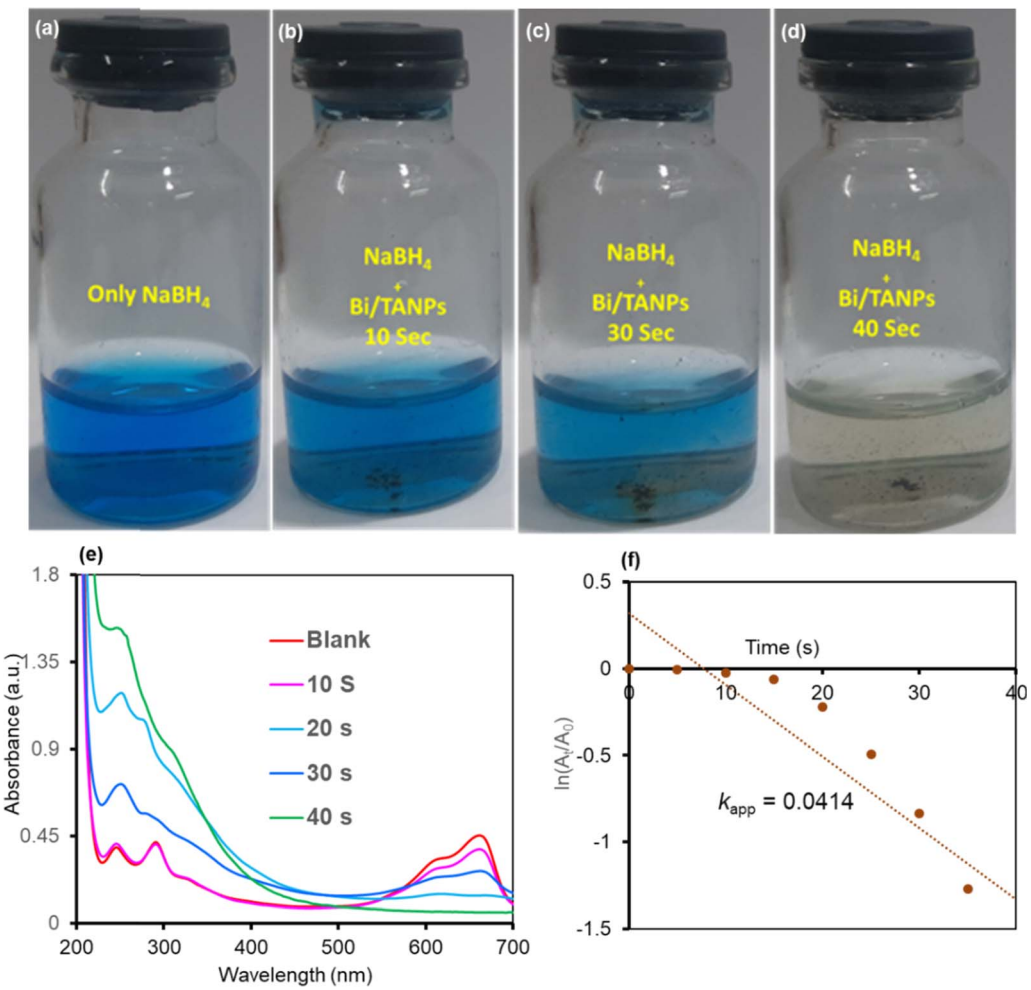

Fig. 6 Discoloration of MB *via* catalytic reduction using Bi/TANPs: (a–d) Optical images of time-dependent change in color; (e) UV-vis spectra during catalytic reduction at different time intervals and (f) pseudo-first-order kinetic plot for the reduction of MB. Conditions: room temperature, reducing agent = 1 mg, catalyst = 0.2 mg, and total volume = 50 mL.

electrons from the former.[54] In the presence of Bi/TANPs, the intensity of maximum absorbance peak at 664 nm is rapidly reduced just after 40 s and the blue color of the aqueous solution of MB became colorless owing to the conversion of MB into LMB, as revealed by the generation of a new peak at 290 nm (Fig. 6e). The rate constant (k) of this reductive degradation reaction was determined from the linear plot of $\ln(A_t/A_0)$ against the reduction time in seconds. The rate constant of MB reduction was calculated from the linear plot of $\ln(A_t/A_0)$ *vs.* time, which is depicted in Fig. 6f, and the data were well fitted with the first-order kinetics. The determined rate constant for the degradation of MB is 0.0414 s^{-1}.

3.6.2 Discoloration of model azo dye, CR *via* catalytic reduction. The catalytic discoloration of CR was also analyzed *via* reductive degradation reaction. Fig. 7a–d show the optical images of the time-dependent degradation of CR by $NaBH_4$ in the absence and presence of Bi/TANP catalyst. When only $NaBH_4$ was present, the reductive degradation of CR was completed after 240 min (Fig. 7a). After the addition of Bi/TANP catalyst, the discoloration through reductive degradation of CR proceeded very faster (Fig. 7b and c). Almost 100% reduction of CR occurred within 60 s and the dye color disappeared (Fig. 7d). The degradation reaction was also observed by UV-vis spectra (Fig. 7e). The aqueous solution of CR showed two absorption bands at 497 and 343 nm assignable to the electronic transitions of n → π* and π → π* in the –N=N– chromophores.[54,55] The degradation of azo groups steadily reduced the strength of two peaks with increasing reaction time, while simultaneously a new peak appeared at 282 nm. Additionally, the weak peak at 255 nm for CR is shifted to 240 nm and the peak intensity was increased with the steady disappearance of a broad CR peak. These two bands at 282 and 240 nm are assignable to the

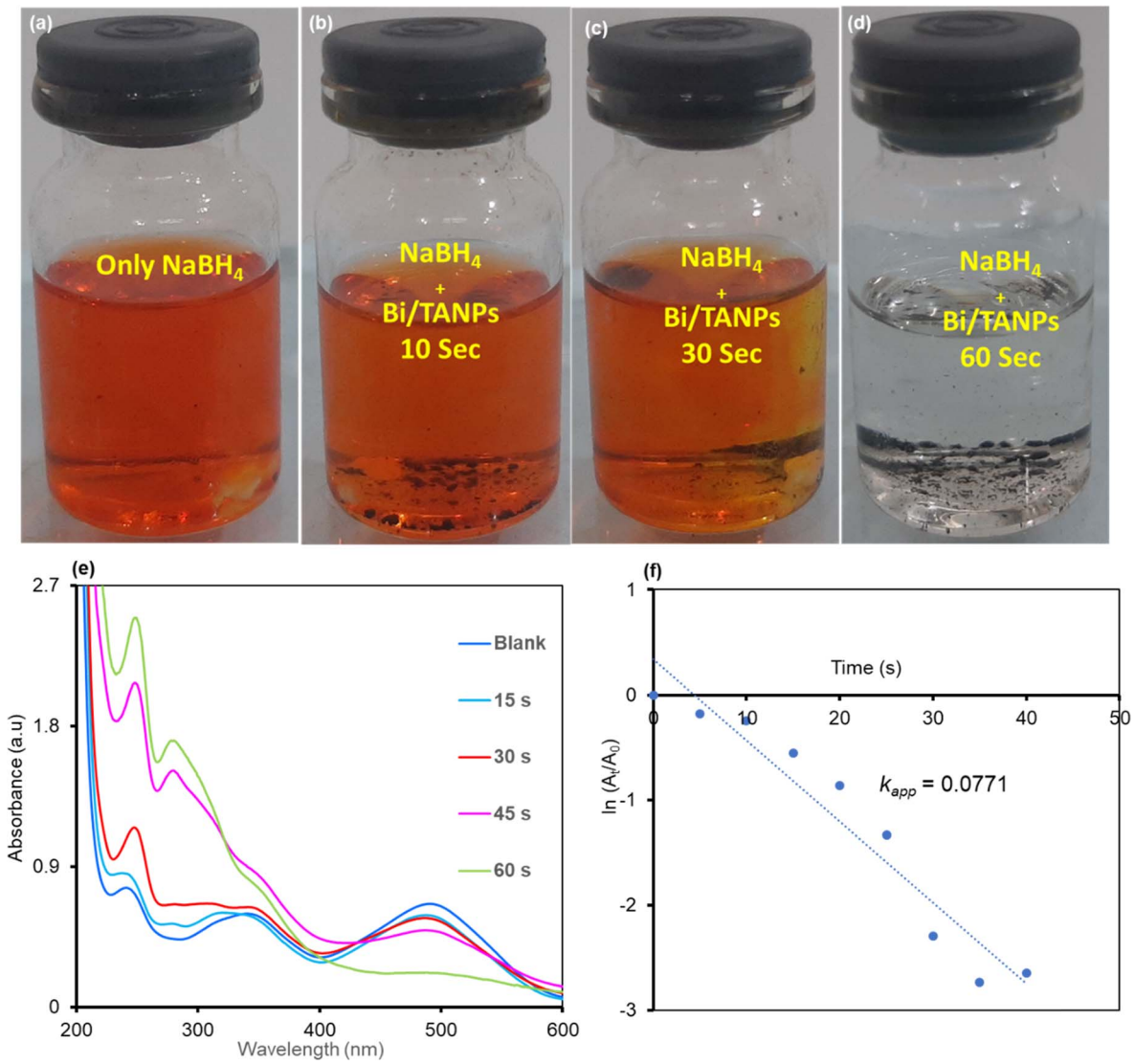

Fig. 7 Discoloration *via* catalytic reduction of CR by Bi/TANPs: (a–d) optical images of time-dependent progress and changes in color; (e) UV-vis spectra during catalytic reduction at different time intervals and (f) kinetic model plot for the reduction reaction. Conditions: room temperature, reducing agent = 1 mg, catalyst = 0.2 mg, and total volume = 50 mL.

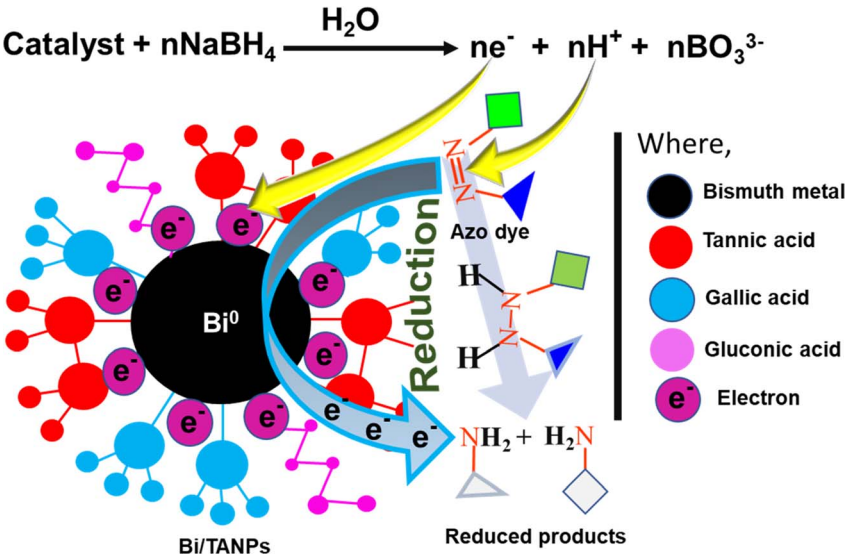

Scheme 3 Schematic of the possible mechanism for azo dye reduction in the presence of Bi/TANPs in an aqueous medium under ambient conditions.

produced hydrazine derivatives such as sodium naphthionate and biphenyl from the catalytic reduction of CR.[58] The reaction kinetic model for the reduction of CR was assessed from the linear relationship between $\ln(A_t/A_0)$ with the reaction time, which is shown graphically in Fig. 7f. The rate constant data of CR discoloration followed the pseudo-first-order kinetic model. The reductive degradation of CR exhibited a rate constant of 0.0771 s^{-1}.

3.6.3 Plausible mechanism for reduction. The catalytic reduction mechanism of azo dyes using Bi/TANPs is shown in Scheme 3. The synthesized Bi/TANPs showed high-efficiency catalytic activity towards the reduction and discoloration of MB and CR due to the following reasons. First, the surface of Bi/TANP catalyst contains TA, gallic acid and gluconic acid molecules that have many phenolic O–H and carboxylate groups. At higher pH, these groups easily transform into anionic as well as quinone moieties. Quinones are considered as electron preservers and redox mediators to speed up the reductive degradation and discoloration of a number of pollutants. These quinone moieties also speed up electron transport to the donor *via* the formation of resonance-stabilized phenoxy radicals.[59] In addition, TA, gallic acid and gluconic acid molecules in Bi/TANPs also served as basic sites that enhanced electron density towards the outer layer of the Bi atoms *via* showing synergetic effects within the stabilized metallic BiNPs, resulting in improved catalytic performance. Besides, TA and gallic acid molecules possess different structural units such as negatively charged phenoxides, carboxylate functionalities, and hydrophobic aromatic nuclei on Bi/TANPs, which can supply specific reactive sites for many adsorbates with high activity and selectivity.[34,36] Second, the mesoporous structure ensures hosting effect to the adsorbate internal space of Bi/TANPs that played a pivotal role for the desired catalytic activity. Consequently, Bi/TANPs relay electrons to the transfer process during the catalytic reduction process. At the beginning of the reduction process, because of electrostatic attraction, azo dye molecules can be transported to the active surface of Bi/TANPs. BH_4^- ions are nucleophilic, whereas the azo dyes are electrophilic in nature with respect to Bi/TANPs. Bi/TANPs accept electrons from BH_4^- ions and transfer them very quickly into the azo-moieties of dye molecules shown in curved arrows.[59,60] Bi/TANPs initiated the catalytic reduction of azo dyes by easily relaying electrons from nucleophilic BH_4^-, whose vital efficiency is connected with the strong electron-injecting ability towards azo-groups of the dye molecules. Electrons required for the reduction reaction are easily localized on the metallic Bi due to the larger atomic size, having more extended and available empty orbitals, where may exist diffuse electron clouds. It is obvious that the outermost electrons are more away from the nucleus and experience weaker attractive forces from the positively charged protons of the nucleus. As a result, the relatively low electron density of the outermost empty shell of metallic Bi^0 still can accept electrons from BH_4^- units. The least repulsion is due to the existence of many vacant outer orbitals of metallic Bi^0 and incoming electrons from BH_4^-. Lastly, the produced H_2 gas from BH_4^- ions circulate in the dispersion medium and catalyst particles as well as faster eliminated reduced products, and decrease the surrounding concentrations of substrate azo dye molecules. Thus, it is a highly efficient catalyst for recyclable catalytic activity.

3.7 Recycling and reusability of catalyst

Recycling and reusability are two important properties for any catalyst, which are practically feasible for easily accessible low-cost operation. Here, recycling experiments were carried out to see the long-term stability and catalytic efficiency of recovered Bi/TANPs for the reductions of organic azo dyes. Fig. 8 shows the efficiencies for the recycling and reusability of Bi/TANPs against MB and CR reduction. It is clear from the diagram

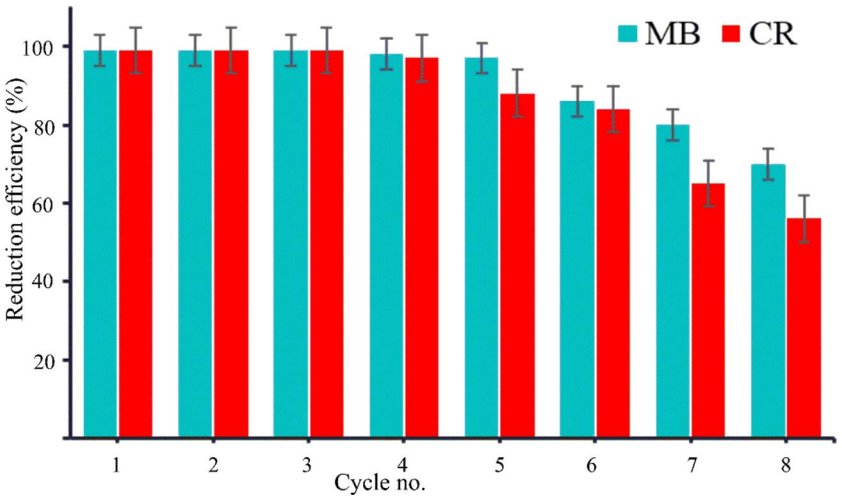

Fig. 8 Recycling efficiency of Bi/TANPs for the reduction of MB and CR in aqueous solutions *via* reductive degradation in the presence of $NaBH_4$ under ambient conditions.

Table 1 Comparison of the catalytic performance of Bi/TANPs with different catalysts reported in the literature for the reduction of azo dyes, namely, MB and CR, in the presence of $NaBH_4$

Serial no.	Dye	Used catalysts	k_{app}	References
1	MB	Fe_3O_4@TA/Ag	0.0685 s^{-1}	26
2	MB	Fe_3O_4@His/Ag	0.270 min^{-1}	54
3	MB	Bimetallic PdO–NiO nanocomposite	0.099 min^{-1}	2
4	MB	PDAMPs	0.843 min^{-1}	55
5	MB	CuO/Ag/Au NCs	0.294 min^{-1}	62
6	MB	Poly(TA)–Cu composites	0.007 min^{-1}	34
7	MB	Fe_3O_4/Cu nanocomposites	0.0089 min^{-1}	63
8	MB	AgNPs	0.3378 min^{-1}	64
9	**MB**	**Bi/TANPs**	**0.0441 s^{-1}**	**This work**
10	CR	AuNPs	0.241 min^{-1}	2
11	CR	Fe_3O_4@PANI@Au	0.80 min^{-1}	65
12	CR	Plant supported AgNPs	0.00214 min^{-1}	66
13	CR	Ag/Ni doped in polymer microgel	0.486 min^{-1}	67
14	CR	*Phoenix dactylifera* seeds	0.45 min^{-1}	68
15	CR	Zero-valent Ag and Cu-based catalyst impregnated in biomass	5.3061 min^{-1}	69
16	CR	Algal biomass-AgNPs	0.37 min^{-1}	70
17	**CR**	**Bi/TANPs**	**0.0771 s^{-1}**	**This work**

that almost 99% of dye molecules are reduced in the first three cycles for both MB and CR. However, a little decreasing trend is observed from the 4th cycle. The decreasing tendency in the catalytic reduction of CR is more pronounced than that of MB due to the functionality, structure, and surface charge variation. These observed efficiencies are clearly higher than our previously designed metal catalysts for the degradation of azo dye compounds.[17] The recyclable reduction efficiencies of Bi/TANPs were retained for MB (53%) and CR (56%) than that of the first cycle even after the 8th cycle.

3.8 Comparison of the catalytic performance

The catalytic performances of Bi/TANPs were compared with other metal-based catalysts reported in the literature, which are given in Table 1. As can be seen from Table 1, most of the supported metals and metal-based catalysts showed lower values for the reduction rate constant of both the azo dyes, MB and CR, than that of our designed Bi/TANP catalyst. For example, bimetallic oxides such as PdO–NiO nanocomposites reduced MB within 5 min.[2] In another work, gold nanoparticles capped with *Salmalia malabarica* gum reduced the MB and CR by 9 min. Fe_3O_4PANI@Au magnetic composites reduced the CR within 6 min.[54,61] While the Bi/TANP nanocatalyst exhibited an excellent rate constant for all the reduction reactions of both azo dyes (MB and CR).

4. Conclusions

In this study, a novel, non-toxic, highly effective and recyclable, low-cost, user-friendly catalyst, Bi/TANP, has been successfully synthesized using abundant TA and glycerin *via*

a new facile aqueous route for reducing azo dye compounds. The prepared Bi/TANPs were pH-responsive and colloidally dispersible in aqueous media. In Bi/TANPs, the presence of functional groups such as O–H, C=O, C=C, C–H, C=O, and C–C was confirmed by FTIR and XPS spectra analyses. The nanocatalyst exhibited crystalline structure, unsmooth morphology, surface porosity, pH-specific activity, and high negative surface charge potential. The XRD result confirmed the formation of metallic Bi/TANPs without the presence of any ionic oxide phase, but XPS and FTIR analyses showed the existence of Bi–O bonds due to the ligation of phenoxide and carboxylate moieties as well as surface air oxidation of Bi atoms during handling, storage and measurements. The Bi/TANP nanocatalyst exhibited high potential affinity and excellent catalytic activity against the reduction of MB and CR in the presence of $NaBH_4$. The kinetics of reduction reactions was monitored by UV-vis absorption spectroscopy. The rate constant was calculated using a linear relationship between $\ln(A_t/A_0)$ and the reduction time in few-ten seconds. The surface functionalization of BiNPs with TA led to faster rate constants of 0.0414 and 0.0771 s^{-1} for the catalytic reduction of MB and CR, respectively. The designed catalyst nanohybrid particles will also be effective against other organic pollutants having nitro, keto, thiol, unsaturated and acid-sensitive groups present in industrial wastewater.

Data availability

All data that are supporting this article, and have been included in the main manuscript and as part of the ESI.†

Author contributions

Md. Ataur Rahman: conducting formal experiments, data acquisitions, curing, analyses, methodology, and writing original draft of the manuscript. Md. Ahasanur Rabbi and Md. Masud Rana: instrumental analyses. Md. Rabiul Karim and Md. Abdul Jalil Miah: project monitoring, review & editing. Hasan Ahmad: investigation, validation, reviewing & editing of the manuscript. Md. Abdur Rahman: conceptualization, investigation, supervision and validation of cured data, critical reviewing & editing of the final manuscript.

Conflicts of interest

The authors declare that they have no known competing financial interests or personal relationships that could have appeared to influence the work reported in this paper.

Acknowledgements

Ataur Rahman is thankful to the Ministry of Science and Technology, Dhaka, Bangladesh for National Science and Technology fellowship during his M. Sc. Thesis. The authors are grateful to the Ministry of Science and Technology, Dhaka, Bangladesh for the special research grant support of the FY 2022–2023 (Project ID: SRG-226679). We are thankful to the Central Science Laboratory, University of Rajshahi, for the FTIR and TGA data support. We acknowledge data assistance from UV-visible spectrophotometer that procured using special allocation from RU authority of the FY 2021–2022.

References

1 P. Barciela, A. Perez-Vazquez and M. A. Prieto, *Food Chem. Toxicol.*, 2023, **178**, 113935.
2 A. G. Ramu and D. Choi, *Sci. Rep.*, 2021, **11**, 22699.
3 B. R. Ganapuram, M. Alle, R. Dadigala, A. Dasari, V. Maragoni and V. Guttena, *Int. Nano Lett.*, 2015, **5**, 215–222.
4 T. R. N. M. Calazans, *et al.*, *Nanoscale Adv.*, 2024, **6**, 3887–3894.
5 B. H. Hameed, A. L. Ahmad and K. N. A. Latiff, *Dyes Pigm.*, 2007, **75**, 143–149.
6 G. Fadillah, T. A. Saleh and S. Wahyuningsih, *J. Mol. Liq.*, 2019, **289**, 111108.
7 B. Monisha, R. Sridharan, P. S. Kumar, G. Rangasamy, V. Gayathri and S. Subhashree, *Chemosphere*, 2023, **313**, 37614.
8 A. Badeenezhad, A. Azhdarpoor, S. Bahrami and S. Yousenejad, *Mol. Simul.*, 2019, **45**, 564–571.
9 D. Yimin, Z. Jiaqi, L. Danyang, N. Lanli, Z. Liling, Z. Yi and Z. Xiaohong, *Colloids Surf., A*, 2018, **550**, 90–98.
10 R. Sun, R. Lv, Y. Li, T. Du, L. Chen, Y. Zhang, X. Zhang, L. Zhang, H. Ma, H. Sun and Y. Qi, *Food Control*, 2023, **145**, 109491.
11 W. Ahlawat, N. Dilbaghi, R. Kumar, N. K. Singhal, A. Kaushik and S. Kumar, *J. Environ. Chem. Eng.*, 2023, **11**, 110268.
12 H. Munawaroh, P. L. Sari, S. Wahyuningsih and A. H. Ramelan, *AIP Conf. Proc.*, 2018, **2014**, 020119.
13 P. Hervés, M. Pérez-Lorenzo, L. M. Liz-Marzán, J. Dzubiella, Y. Lu and M. Ballauff, *Chem. Soc. Rev.*, 2012, **41**, 5577.
14 B. Baruah, G. J. Gabriel, M. J. Akbashev and M. E. Booher, *Langmuir*, 2013, **29**, 4225–4234.
15 S. Wunder, F. Polzer, Y. Lu, Y. Mei and M. Ballauff, *J. Phys. Chem. C*, 2010, **114**, 8814–8820.
16 J. A. Johnson, J. J. Makis, K. A. Marvin, S. E. Rodenbusch and K. J. Stevenson, *J. Phys. Chem. C*, 2013, **117**, 22644–22651.
17 M. Z. Sarker, M. M. Rahman, H. Minami, T. Suzuki, M. A. Rahman, A. Khan, S. M. Hoque and H. Ahmad, *Colloids Surf., A*, 2022, **647**, 129044.
18 H. He, Q.-Q. Zhu, Y. Yan, H.-W. Zhang, Z.-Y. Han, H. Sun, J. Chen, C.-P. Li, Z. Zhang and M. Du, *Appl. Catal., B*, 2022, **302**, 120840.
19 R. Mohami, A. Shakeri and M. Nasrollahzadeh, *Sep. Purif. Technol.*, 2022, **285**, 120373.
20 Y. Fu, W. Kong, B. Pan, C. Yuan, S. Li, H. Zhu and J. Zhang, *J. Environ. Chem. Eng.*, 2021, **9**, 105790.
21 Y. Liang, J. Manioudakis, J.-R. Macairan, M. S. Askari, P. Forgione and R. Naccache, *ACS Omega*, 2019, **4**, 14955–14961.
22 A. L. Brown, P. C. Naha, V. Benavides-Montes, H. I. Litt, A. M. Goforth and D. P. Cormode, *Chem. Mater.*, 2014, **26**, 2266–2274.

23 P. Lei, P. Zhang, Q. Yuan, Z. Wang, L. Dong, S. Song, X. Xu, X. Liu, J. Feng and H. Zhang, *ACS Appl. Mater. Interfaces*, 2015, **7**, 26346–26354.
24 F. Wang, R. Tang, H. Yu, P. C. Gibbons and W. E. Buhro, *Chem. Mater.*, 2008, **20**, 3656–3662.
25 H. Yu, P. C. Gibbons and W. E. Buhro, *J. Mater. Chem.*, 2004, **14**, 595.
26 C. Xing, W. Huang, Z. Xie, J. Zhao, D. Ma, T. Fan, W. Liang, Y. Ge, B. Dong, J. Li and H. Zhang, *ACS Photonics*, 2018, **5**, 621–629.
27 R. K. Verma, K. Kumar and S. B. Rai, *J. Colloid Interface Sci.*, 2013, **390**, 11–16.
28 S. C. Warren, A. C. Jackson, Z. D. Cater-Cyker, F. J. DiSalvo and U. Wiesner, *J. Am. Chem. Soc.*, 2007, **129**, 10072–10073.
29 F. Wang and W. E. Buhro, *Small*, 2010, **6**, 573–581.
30 W. Ye, J. Yu, Y. Zhou, D. Gao, D. Wang, C. Wang and D. Xue, *Appl. Catal., B*, 2016, **181**, 371–378.
31 L. N. Borovikova, I. V. Polyakova, E. M. Korotkikh, V. K. Lavrent'ev, A. I. Kipper and O. A. Pisarev, *Russ. J. Phys. Chem. A*, 2018, **92**, 2253–2256.
32 F. Xia, X. Xu, X. Li, L. Zhang, L. Zhang, H. Qiu, W. Wang, Y. Liu and J. Gao, *Ind. Eng. Chem. Res.*, 2014, **53**, 10576–10582.
33 A. M. G. C. Dias, A. Hussain, A. S. Marcos and A. C. A. Roque, *Biotechnol. Adv.*, 2011, **29**, 142–155.
34 N. Sahiner, S. Sagbas and N. Aktas, *RSC Adv.*, 2015, **5**, 18183–18195.
35 C. W. Lim and I. S. Lee, *Nano Today*, 2010, **5**, 412–434.
36 T. Ahmed, *J. Nanotechnol.*, 2014, **2014**, 954206.
37 H. Veisi, S. B. Moradi, A. Saljooqi and P. Safarimehr, *Mater. Sci. Eng., C*, 2019, **100**, 445–452.
38 G. Sathishkumar, K. Gopinath, K. Zhang, E.-T. Kang, L. Xu and Y. Yu, *J. Mater. Chem. B*, 2022, **10**, 2296–2315.
39 H. Ullah, S. Qamar, F. Khan, F. Raheem, A. Shamim, I. Uddin, Z. U. Rehman, F. Ahmad and M. R. Shah, *J. Ongoing Chem. Res.*, 2019, **4**, 24–31.
40 A. D. Nowicki, N. Mordvinova and A. Roucoux, in *Nanoparticles in Catalysis*, ed. K. Philippot and A. Roucoux, Wiley, 1st edn, 2021, pp. 43–71.
41 A. Dutta and S. K. Dolui, *Appl. Surf. Sci.*, 2011, **257**, 6889–6896.
42 M.-O. Simon and C.-J. Li, *Chem. Soc. Rev.*, 2012, **41**, 1415–1427.
43 W. Silen, T. Machen and J. Forte, *Am. J. Physiol.*, 1975, **229**, 721–730.
44 T. Liu, D. R. Baek, J. S. Kim, S.-W. Joo and J. K. Lim, *ACS Omega*, 2020, **5**, 16246–16254.
45 W. U. Rehman, U. Farooq, M. Z. Yousaf and A. Altalb, *Materials*, 2023, **16**, 6628.
46 S. Eslami, M. A. Ebrahimzadeh and P. Biparva, *RSC Adv.*, 2018, **8**, 26144–26155.
47 M. A. Rahman and B. Ochiai, *RSC Adv.*, 2022, **12**, 8043.
48 M. A. Rahman, Y. Matsumura, S. Yano and B. Ochiai, *ACS Omega*, 2018, **3**, 961–972.
49 Z. Xia, A. Singh, W. Kiratitanavit, R. Mosurkal, J. Kumar and R. Nagarajan, *Thermochim. Acta*, 2015, **605**, 77–85.
50 N. Sheoran, A. Kumar, V. Kumar and A. Banerjee, *J. Supercond. Novel Magn.*, 2020, **33**, 2017–2029.
51 G. A. Gomez-Iriarte, A. Pentón-Madrigal, L. A. S. De Oliveira and J. P. Sinnecker, *Materials*, 2022, **15**, 4285.
52 P. Kumar, J. Singh and A. C Pandey, *RSC Adv.*, 2013, **3**, 2313.
53 M. E. Flores, P. S. Jacinto, C. M. R. S. Germán, L. R. Vázquez, R. B. Urby and N. C. Castro, *Front. Mater. Sci.*, 2016, **10**, 394–404.
54 M. Chen, P. Liu, C. Wang, W. Ren and G. Diao, *New J. Chem.*, 2014, **38**, 4566–4573.
55 M. Amir, U. Kurtan and A. Baykal, *J. Ind. Eng. Chem.*, 2015, **27**, 347–353.
56 M. Z. Sarker, M. M. Rahman, H. Minami, T. Suzuki, M. K. Hossain and H. Ahmad, *Colloids Surf., A*, 2021, **617**, 126403.
57 M. J. Uddin, M. A. Islam, S. A. Haque, S. Hasan, M. S. A. Amin and M. M. Rahman, *Int. Nano Lett.*, 2012, **2**, 19.
58 N. Cheval, N. Gindy, C. Flowkes and A. Fahmi, *Nanoscale Res. Lett.*, 2012, **7**, 182.
59 K. Iqbal, A. Iqbal, A. M. Kirillov, B. Wang, W. Liu and Y. Tang, *J. Mater. Chem. A*, 2017, **5**, 6716–6724.
60 Y. Zheng and A. Wang, *J. Mater. Chem.*, 2012, **22**, 16552.
61 X. Cui, Y. Zheng, M. Tian and Z. Dong, *Appl. Surf. Sci.*, 2017, **416**, 103–111.
62 A. Sankaran, K. Kumaraguru and B. Balraj, *J. Inorg. Organomet. Polym. Mater.*, 2021, **31**, 151–161.
63 Z. Wang, S. Zhai, B. Zhai and Q. An, *Eur. J. Inorg. Chem.*, 2015, **2015**, 1692–1699.
64 S. A. Ogundare, T. O. Adesetan, G. Muungani, V. Moodley, J. F. Amaku, *et al.*, *Environ. Sci.: Adv.*, 2023, **2**, 247–256.
65 Y. Zhu, X. Zhou, D. Chen, *et al.*, *Sci. China: Technol. Sci.*, 2017, **60**, 749–757.
66 M. Ismail, M. I. Khan, S. B. Khan, K. Akhtar, M. A. Khan and A. M. Asiri, *J. Mol. Liq.*, 2018, **268**, 87–101.
67 M. Arif, *RSC Adv.*, 2023, **13**, 3008.
68 D. Pathania, A. Sharma and Z.-M. Siddiqi, *J. Mol. Liq.*, 2016, **219**, 359–367.
69 S. A. Shah, Z. Ahmad, S. A. Khan, Y. O. Al-Ghamdi, E. M. Bakhsh, N. Khan, M. Ur Rehman, M. Jabli and S. B. Khan, *J. Organomet. Chem.*, 2021, **938**, 121756.
70 S. Panigrahi, S. S. Priyadarshini, P. M. Mishra, *et al.*, *Water, Air, Soil Pollut.*, 2024, **235**, 209.